

Microscopic calculations of medium effects for 200-MeV (p,p') reactions

F. Sammarruca

University of Idaho, Moscow, ID 83843 USA

E.J. Stephenson and K. Jiang

Indiana University Cyclotron Facility, Bloomington, IN 47408 USA

Abstract

We examine the quality of a G-matrix calculation of the effective nucleon-nucleon (NN) interaction for the prediction of the cross section and analyzing power for 200-MeV (p,p') reactions that populate natural parity states in ^{16}O , ^{28}Si , and ^{40}Ca . This calculation is based on a one-boson-exchange model of the free NN force that reproduces NN observables well. The G-matrix includes the effects of Pauli blocking, nuclear binding, and strong relativistic mean-field potentials. The implications of adjustments to the effective mass ansatz to improve the quality of the approximation at momenta above the Fermi level will be discussed, along with the general quality of agreement to a variety of (p,p') transitions.

1. Introduction

One of the goals of nuclear physics is to describe the structure of nuclei and the dynamics of nuclear reactions in terms of the underlying interaction between nucleons. But from a practical standpoint a microscopic calculation of the many-body system is not a viable option. Thus a major quest in studies of the nuclear many-body problem is the construction of an effective nucleon-nucleon interaction, modified so as to account for the presence of the many-body environment, that can be used in a simplified treatment of the properties of nuclear matter or nuclear reactions.

The most commonly included many-body mechanisms arise from Pauli blocking and nuclear binding, and are the main aspects of what is known as the Brueckner G-matrix approach [1-6]. Its relativistic extension in which the nuclear mean field is characterized by strong, competing scalar and vector fields, is known as Dirac-Brueckner theory [7-10] and has also become a rather established method. This scheme accounts in a more natural way for the size of the spin-orbit splitting seen in nuclear states. We will refer to all of these effects as “conventional” medium modifications.

More exotic medium effects have been proposed. Perhaps the most extensively discussed are those arising from changes in the QCD vacuum induced by increasing nuclear matter density, which are expected to lower both nucleon and meson effective masses in the medium [11,12]. Based in part on considerations of quark condensates in nuclear matter [13], this reduction is expected to be about 20% for the meson masses at normal nuclear matter densities, and would represent a precursor of the transition to a chirally restored phase at higher temperatures and densities. Since the pion is a Goldstone boson, its mass would change only very slowly with increasing density. For the tensor interaction which arises from the competing contributions of the long-range pion and the short-range ρ -meson, a lowering of the ρ -meson mass would result in a reduced tensor attraction at medium range. This should be observable in nucleon-induced reactions such as (p,p') inelastic scattering or (p,n) charge exchange through a measurement of the degree of spin-flip in polarization transfer [14,15]. Charge-exchange quasi-free scattering consistently shows a lowering of the ratio of spin-longitudinal to transverse responses relative to RPA calculations, a result that has been interpreted as evidence for a weakening of the pionic component in nuclei [16]. Comparable results have been reported for discrete isovector transitions that also suggest a weakened tensor force. The polarization transfer coefficient D_{NN} , normally negative in the plane-wave limit [17], moves toward zero [18,19] or becomes positive [20], for example.

In this paper, we will establish a basis from which the question of exotic contributions to the medium-dependent effective interaction can be explored, in particular through the spin dependence of proton elastic scattering, (p,p') inelastic scattering, and (p,n) reactions. We will begin with a one-boson-exchange (OBE) representation of the nucleon-nucleon (NN) interaction that provides an excellent reproduction of the NN observables below pion production threshold. Then the density-dependent effective interaction is obtained by solving the Bethe-Goldstone equation in infinite nuclear matter. It contains all the conventional effects as

defined above. Next the resulting G-matrix is converted to a Yukawa-function form [21] for use in Distorted Wave Impulse Approximation (DWIA) calculations. The early sections of this paper describe these models, most of which have been explained in greater detail elsewhere, except for the transformation from t-matrix to Yukawa-function form. This information is included here to support the observations and discussion later in the paper, some of which are unique to our application. Section 2 describes the OBE model, which is an updated version of the Bonn interaction [22], and Section 3 outlines the G-matrix solution. The transformation is described in Section 4, and shown in complete form in the Appendix. Details of the DWIA calculations are given in Section 5. For the calculations in this paper we will make use of the LEA program from Kelly [23]. This program operates in coordinate space and assumes zero-range exchange. The effect of this will be discussed in more detail later in the paper.

The treatment of conventional medium effects through a G-matrix for use in (p,p') or (p,n) reactions is certainly not new. Pauli blocking and nuclear binding effects have been used to create interactions that have received wide examination [24-27]. While producing effects on the NN interaction that are qualitatively similar, the size of the predicted changes differs from author to author. We will examine the central issues involved in the so-called “effective mass approximation,” a crucial step in the G-matrix method. From studies of nuclear matter, effective in-medium nucleon masses have been previously determined [22]. However, for nucleons with energies in the continuum, we find that this approximation works best for a different choice of the effective masses. The consequences of this will be explored in Section 6. There we will also illustrate how variations in this approximation affect the calculation of a folding model $(t\rho)$ optical potential and (p,p') observables.

Relatively few relativistic calculations of medium effects have been performed for the case of inelastic scattering. Here we will compare our work to that of Furnstahl and Wallace [28], where the nucleons in the nucleus are described by Dirac bound states. These authors consider specific finite nuclei, and point out that the density dependent effects for the elastic scattering channel are less than those for the reaction channels because of the identity between initial and final states in the first case. In our paper, the G-matrix is constructed for infinite nuclear matter, and no such distinction exists, namely, we use the same effective interaction for elastic and inelastic scattering. The implications of this difference in approach will also be examined in Section 6.

Since the primary purpose of this paper is to examine the treatment of conventional medium effects, we will compare our predictions in Section 7 to measurements of the cross section and analyzing power for natural-parity, isoscalar (p,p') transitions where these effects are largest. We have chosen the data of Seifert [29] on ^{16}O and ^{40}Ca (200 MeV) and Chen [30] on ^{28}Si (180 MeV) since these are the same energies and targets that will appear in a future consideration of exotic medium effects for polarization transfer measurements. For natural parity transitions, polarization transfer measurements do not add new information to the analysis beyond that contained in the cross section and analyzing power [31] and will not be considered here. On the basis of these comparisons we will then be able to evaluate the theoretical tools presented here for dealing

with the nuclear medium.

2. The nucleon-nucleon interaction

The starting point for a microscopic calculation of (p,p') reactions is a realistic free-space NN interaction which reproduces well NN scattering observables. Below pion production threshold, we would expect that a one-boson-exchange basis would prove adequate. This is a very popular and quantitative reduction of a more comprehensive model which would contain multiple meson-exchange diagrams [22].

In this work, we will use an updated version of the Bonn-B potential [22]. We have chosen pseudovector coupling for the pion, and will solve for the NN interaction through the use of the Thompson equation. The major bosons in the model are: (a) the pseudoscalar pion, which is the lightest and hence longest ranged of the mesons and which provides most of the attractive tensor force, (b) the ρ vector meson, a 2-pion P-wave resonance that provides a short-range repulsive tensor force, (c) the ω vector meson, a 3-pion resonance that creates a strong, repulsive central force at short range and that contributes to the spin-orbit force, and (d) the fictitious isoscalar-scalar σ meson that represents 2-pion S-wave exchange and that contributes to the medium range attraction necessary to bind the nucleus.

These mesons are coupled to the nucleon through the Lagrangians for the pseudovector (pv), scalar (s), and vector (v) fields:

$$\mathcal{L}_{pv} = -\frac{f_{ps}}{m_{ps}}\bar{\psi}\gamma^5\gamma^\mu\psi\partial_\mu\phi^{(ps)} \quad (1)$$

$$\mathcal{L}_s = g_s\bar{\psi}\psi\phi^{(s)} \quad (2)$$

$$\mathcal{L}_v = -g_v\bar{\psi}\gamma^\mu\psi\phi_\mu^{(v)} - \frac{f_v}{4m}\bar{\psi}\sigma^{\mu\nu}\psi(\partial_\mu\phi_\nu^{(v)} - \partial_\nu\phi_\mu^{(v)}) \quad (3)$$

with ψ the nucleon and $\phi_{(\mu)}^{(\alpha)}$ the meson fields (notation and conventions as in Ref. [22]). For isovector (isospin = 1) mesons such as the π and ρ , $\phi^{(\alpha)}$ is to be replaced by $\tau\cdot\phi^{(\alpha)}$ with τ the usual Pauli matrices acting in isospin space.

The OBE amplitudes are derived from the Lagrangians in Eqs. (1) through (3). For example, the contribution to the potential from the isoscalar-scalar σ meson is

$$\langle\mathbf{q}'\lambda'_1\lambda'_2|V_s^{OBE}|\mathbf{q}\lambda_1\lambda_2\rangle = -g_s^2\bar{u}(\mathbf{q}',\lambda'_1)u(\mathbf{q},\lambda_1)\bar{u}(-\mathbf{q}',\lambda'_2)u(-\mathbf{q},\lambda_2)\frac{\mathcal{F}_s[(\mathbf{q}'-\mathbf{q})^2]^2}{(\mathbf{q}'-\mathbf{q})^2+m_s^2} \quad (4)$$

where λ_i (λ'_i), with $i = 1, 2$, denotes the helicity of the incoming (outgoing) nucleons. $\mathcal{F}_s[(\mathbf{q}'-\mathbf{q})^2]$ is a monopole form factor that simulates the short-range physics governed by quark-gluon dynamics,

$$\mathcal{F}_s[(\mathbf{q}'-\mathbf{q})^2] = \frac{\Lambda_s^2 - m_s^2}{\Lambda_s^2 + (\mathbf{q}'-\mathbf{q})^2}, \quad (5)$$

with Λ_s the cutoff mass of the isoscalar-scalar meson. The Dirac spinors are normalized covariantly to

$$\bar{u}(\mathbf{q},\lambda)u(\mathbf{q},\lambda) = 1. \quad (6)$$

Table 1. OBE meson properties

meson	mass (MeV)	coupling ($g^2/4\pi$)	cutoff (MeV)
π	138.03	13.8	1700
η	548.8	3	1500
ρ	769	0.99 ($f_\rho/g_\rho = 6.1$)	1300
ω	782.6	22	1500
σ ($T = 0$)	550	5.966	2000
σ ($T = 1$)	550	8.5	2000

Table 2. σ meson couplings

partial wave	coupling ($g^2/4\pi$)
3P_1	8.9
1D_2	10.05
3P_2	9.11
3F_3	13.5

The OBE amplitudes for other mesons are given in Refs. [22,32]. The OBE potential is the sum of the OBE amplitudes for all the exchanged mesons.

Since the parameters of the original Bonn-B interaction were determined about a decade ago, there has been substantial progress in both high-precision measurements of NN scattering and phase shift analyses. Since a good fit to the NN data is a crucial prerequisite for an evaluation of the quality of the (p,p') calculations, the parameters of the model have been adjusted to bring the predictions into better accord with current phase shift analyses from the Nijmegen group up to 325 MeV [33]. The σ meson is different in the two isospin channels. As a consequence of this extra degree of freedom, the other scalar meson, the δ meson, becomes unimportant and is therefore suppressed. The values for the masses, coupling constants, and cutoff parameters for these mesons are given in Table 1. This scheme is not fully satisfactory in the $T = 1$ channel. So in a manner similar to that used in the construction of the (charge-dependent) CD-Bonn interaction [34], adjustments have been made to the σ -meson coupling constant for some individual partial waves. These altered values are given in Table 2.

Generally, the agreement with NN data around 200 MeV was found to be excellent.

3. The G-matrix calculation

3a. Conventional Brueckner theory

It has been almost fifty years since Brueckner and collaborators [1] initiated work on a method, further developed by Bethe and Goldstone [2,3], to calculate the properties of nuclear matter. Systematic calculations applying Brueckner's theory started in the late 1960's and continued throughout the 1970's [4-6]. For a review, see Ref. [22].

The Brueckner-Bethe-Goldstone model is based on the idea that nucleons in nuclear matter move in a single-particle potential arising from the interaction with all the other nucleons. For practical reasons, infinite nuclear matter systems are typically used in studies of the nuclear many-body problem as a working approximation to actual finite systems.

Kinematics for the two interacting nucleons are defined in terms of the following momentum vectors. Consider a nucleon with momentum \mathbf{k}_1 colliding with another of momentum \mathbf{k}_2 embedded in infinite nuclear matter. The Fermi sea is defined by the Fermi momentum k_F . If \mathbf{k}_1 and \mathbf{k}_2 are the momenta of two nucleons in the nuclear matter rest frame, it is convenient to introduce the relative momentum

$$\mathbf{k} = \frac{1}{2}(\mathbf{k}_1 - \mathbf{k}_2) \quad (7)$$

and one-half of the center-of-mass momentum

$$\mathbf{P} = \frac{1}{2}(\mathbf{k}_1 + \mathbf{k}_2) . \quad (8)$$

Conversely, we have

$$\mathbf{k}_{1,2} = \mathbf{P} \pm \mathbf{k} . \quad (9)$$

The effective two-nucleon interaction in infinite nuclear matter, or G-matrix, is a solution of the Bethe-Goldstone equation

$$\langle \mathbf{k} | \mathbf{G}(\mathbf{P}, k_F) | \mathbf{k}_0 \rangle = \langle \mathbf{k} | V | \mathbf{k}_0 \rangle - \int \frac{d^3 k'}{(2\pi)^3} \frac{\langle \mathbf{k} | V | \mathbf{k}' \rangle Q(\mathbf{k}', \mathbf{P}, k_F) \langle \mathbf{k}' | \mathbf{G}(\mathbf{P}, k_F) | \mathbf{k}_0 \rangle}{E(\mathbf{P}, \mathbf{k}') - E_0 - i\epsilon} \quad (10)$$

with \mathbf{k}_0 , \mathbf{k} , and \mathbf{k}' the initial, final, and intermediate relative momenta, respectively [defined in Eq. (7)], and V is the NN OBE potential defined in the previous section. E is the energy of the two-nucleon system, and E_0 is the same quantity on-shell. Thus

$$E(\mathbf{P}, \mathbf{k}) = e(\mathbf{P} + \mathbf{k}) + e(\mathbf{P} - \mathbf{k}) \quad (11)$$

with e the single-particle energy in nuclear matter.

Eq. (10) is density-dependent due to the presence of the Pauli projection operator Q , defined by

$$Q(\mathbf{k}, \mathbf{P}, k_F) = \begin{cases} 1, & \text{if } k_{1,2} > k_F \\ 0, & \text{otherwise} \end{cases} \quad (12)$$

with $k_{1,2}$ the magnitude of the momenta of Eq. (9). Q prevents scattering into occupied intermediate states.

To make the calculation more tractable, $Q(\mathbf{k}, \mathbf{P}, k_F)$ is usually replaced by its angle average,

$$\bar{Q}(k, P, k_F) = \frac{\int d\Omega Q(\mathbf{k}, \mathbf{P}, k_F)}{\int d\Omega} \quad (13)$$

with $d\Omega$ the solid angle element. The angle-averaged Pauli function approaches the exact value only when the center-of-mass momentum, P , in Eq. (8), approaches zero. In the context of nuclear matter saturation (negative incident energies), it has been shown that the angle averaging is a good approximation [35]. It has also been demonstrated that the quality of this approximation is still good for positive energies up to about 300 MeV and normal nuclear matter densities [36].

In nuclear matter, the energy of a single particle with momentum p , which appears in the energy-denominator of Eq. (10), is also density-dependent and defined by

$$e(p) = T(p) + U(p) , \quad (14)$$

where $T(p)$ is the kinetic energy and $U(p)$ is a single-particle potential generated by the average interaction of all the nucleons in the Fermi sea. For nucleons below and above the Fermi level we define

$$U(p) = \langle p|U|p\rangle = Re \sum_{q \leq k_F} \langle pq|G|pq - qp\rangle \quad (15)$$

with $|p\rangle$ and $|q\rangle$ single particle momentum, spin, and isospin states.

Thus, the propagator in Eq. (10) depends on $U(p)$ through the single-particle energy ϵ in Eq. (14). Consequently, the determination of G depends on the choice of $U(p)$. Since the potential $U(p)$ must be determined from the reaction matrix through Eq. (15), which depends on G , a solution for both quantities must be reached in a self-consistent way.

For reasons of numerical convenience, we will use the *effective mass ansatz* [5], which is equivalent to replacing the single-particle energy with

$$\frac{p^2}{2m} + U(p) \rightarrow \frac{p^2}{2m^*} + U_0 . \quad (16)$$

This way, the potential $U(p)$ is parametrized in terms of an effective mass m^* and a constant U_0 . Eq. (16) implies

$$U(p) = \frac{1}{2} \frac{m - m^*}{mm^*} p^2 + U_0 , \quad (17)$$

that is, the potential $U(p)$ has been fitted with a quadratic function of p . Starting from some initial values for m^* and U_0 , we proceed to calculate G from Eq. (10). From the resulting G , the potential $U(p)$ is then calculated via Eq. (15) and parametrized in terms of a new set of m^* and U_0 . The procedure is repeated until the values of m^* and U_0 have converged.

The on-shell G -matrix is a set of complex numbers associated with each of the partial wave quantum numbers usually used for NN phase shifts. Since we are below pion production threshold, these can be

checked for agreement with unitarity. Agreement is excellent at zero density, and represents one verification of the numerical accuracy of the program. However unitarity, particularly for the lower partial waves, is not obeyed as the nuclear density increases. In some cases, the inelasticity parameter differed from one by as much as 18% at full nuclear density. Respecting these violations of unitarity in the subsequent transformation to an effective NN interaction is crucial, especially for the imaginary terms. Without that, even qualitative agreement with previous density-dependent analyses would have been impossible.

Finally, from the self-consistently produced G-matrix, scattering parameters (positive energies) or the bound state properties (negative energies) can be predicted. However, nuclear matter calculations based on this approach have been only partially successful, failing to predict correctly nuclear matter saturation. Typically the saturation density is too high for reasonable binding energies. Different calculations that change some aspect of the model or use another NN potential give somewhat different predictions, but all of them fail to reproduce simultaneously the correct combination of saturation energy and density [22]. Since the calculation at this stage resembles other work on nuclear matter effects, we will use it later to establish our method and refer to it as the Brueckner-Hartree-Fock (BHF) theory. One aspect that is not included in this framework is an explicit consideration of the effects of the lower components when the nucleon is treated as a Dirac spinor. This extended calculation, which we will refer to as the Dirac-Brueckner-Hartree-Fock (DBHF) theory, is described in the next subsection.

3b. The relativistic approach

In the early 1970's, a relativistic approach to nuclear structure was developed by Miller and Green [37] to study the ground states of nuclei. This was successful in explaining the single-particle energy levels, and in particular the spin-orbit splitting. In 1974, Walecka [38] published the Dirac-Hartree model for highly condensed matter. Later, Clark and collaborators [39] applied a Dirac equation containing a scalar and the time-like component of a vector field to proton-nucleus scattering. The Dirac-Hartree and Dirac-Hartree-Fock approach to nuclear matter and finite nuclei were further developed by Brockmann [40], Horowitz and Serot [41], and Serot and Walecka [42]. Finally, a relativistic extension of Brueckner theory was proposed by Shakin *et al.* [7], and further developed by Brockmann and Machleidt [8], and Horowitz and Serot [9]. Extensive applications and a review have been presented by ter Haar and Malfliet [10].

A nucleon in the nuclear medium can be viewed as a 'bare' nucleon that is 'dressed' as a consequence of its effective two-body interactions with the other nucleons. Then, the bare and the dressed nucleon propagators are related through the Dyson equation

$$\mathcal{G}(p) = \mathcal{G}^0(p) + \mathcal{G}^0(p)U(p)\mathcal{G}(p) \quad (18)$$

where $U(p)$ is the relativistic self-energy. Eq. (18) has the formal solution

$$\mathcal{G}(p) = (\not{p} - m - U(p))^{-1} . \quad (19)$$

To be consistent with symmetry requirements, the self-energy must have the general Lorentz structure [43]

$$U(p) = U_S(p) + \gamma_0 U_V^0(p) - \boldsymbol{\gamma} \cdot \mathbf{p} U_V(p) \quad (20)$$

where $U_S(p)$ and $U_V(p)$ are an attractive scalar field and a repulsive vector field, respectively, and $U_V^0(p)$ is the timelike component of the vector field. It has been shown [43] that $U_V(p)$ is much smaller than either $U_S(p)$ and $U_V^0(p)$. Thus we can write

$$U(p) \approx U_S(p) + \gamma^0 U_V^0(p) . \quad (21)$$

Now, substituting Eq. (21) into Eq. (19) leads to the following definitions:

$$m^*(p) = m + U_S(p) \quad (22)$$

and

$$(p^0)^* = p^0 - U_V^0(p) , \quad (23)$$

which enables us to write the nucleon propagator in nuclear matter, Eq. (19), as

$$\mathcal{G}(p) = (\not{p}^* - m^*)^{-1} . \quad (24)$$

Thus the Dirac equation in nuclear matter

$$(\not{p} - m - U(p))u(\mathbf{p}, s) = 0 \quad (25)$$

can be written simply as

$$(\not{p}^* - m^*)u(\mathbf{p}, s) = 0 \quad (26)$$

with the positive energy solution

$$u(\mathbf{p}, s) = \left(\frac{\epsilon_p^* + m^*}{2m^*} \right)^{1/2} \begin{pmatrix} \mathbf{1} \\ \frac{\boldsymbol{\sigma} \cdot \mathbf{p}}{\epsilon_p^* + m^*} \end{pmatrix} \chi_s \quad (27)$$

where χ_s is a Pauli spinor, and

$$\epsilon_p^* = (m^{*2} + \mathbf{p}^2)^{1/2} . \quad (28)$$

$u(\mathbf{p}, s)$ is formally identical to a free-space spinor, but with m replaced by m^* .

As mentioned earlier, Dirac spinors use the covariant normalization $u\bar{u} = 1$. However physical nucleon states must be normalized by $w w^\dagger = 1$, where $w = \sqrt{m^*/\epsilon^*} \times u$.

From Eq. (21), the single-particle potential is

$$U(p) = \frac{m^*}{\epsilon_p^*} \langle p | U_S + \gamma^0 U_V^0 | p \rangle \quad (29)$$

where $|p\rangle$ is a Dirac spinor as in Eq. (27) and $\langle p|$ the adjoint spinor. In analogy with the usual Hartree-Fock definition,

$$U(p) = Re \sum_{q \leq k_F} \frac{m^{*2}}{\epsilon_p^* \epsilon_q^*} \langle pq | G | pq - qp \rangle , \quad (30)$$

which is similar to the (non-relativistic) Brueckner-Hartree-Fock definition of the single-particle potential in Eq. (15). This situation is now technically identical to the one encountered in the non-relativistic case. Eq. (30) and the relativistic (Thompson form) G-matrix equation (with the potential V written in terms of the in-medium spinor from Eq. (27)) must be solved self-consistently for G and $U(p)$. $U_S(p)$ and $U_V^0(p)$ are momentum dependent, but to a good approximation they can be taken as constant [7,9]. Thus, the single particle potential becomes

$$U(p) = \frac{m^*}{\epsilon_p^*} U_S + U_V^0 . \quad (31)$$

Eq. (31) is a consequence of Eq. (29) together with our normalization conventions: $u\bar{u} = 1$ and $u u^\dagger = \epsilon_p^*/m^*$, with $\bar{u} = u^\dagger \gamma^0$. In analogy with Eq. (17), Eq. (31) parametrizes the energy of a particle in nuclear matter in terms of two constants, which is clearly equivalent to the effective mass ansatz used in the previous subsection for the non-relativistic case.

The main difference between BHF and DBHF is that for DBHF the nucleon wave function, Eq. (27), is obtained self-consistently, while in BHF the free-space solution is used. Such a difference turns out to be of fundamental importance. As a consequence of the reduced nucleon mass, the lower component of the nucleon spinor is larger than in free space. This is well known to produce a density-dependent, repulsive many-body effect, with the result that saturation can be predicted at the correct density [7]. To demonstrate how this happens, consider a vertex with a scalar coupling, such as the one involved in σ -exchange. Using Eq. (27), we have

$$\bar{u}(\mathbf{p}', s') u(\mathbf{p}, s) \propto \chi_s' \left(1 - \left(\frac{\boldsymbol{\sigma} \cdot \mathbf{p}}{\epsilon_p^* + m^*} \right) \left(\frac{\boldsymbol{\sigma} \cdot \mathbf{p}'}{\epsilon_p'^* + m^*} \right) \right) \chi_s , \quad (32)$$

which is one of the two vertices involved in the (attractive) σ -exchange potential diagram of Eq. (4). As the nucleon mass decreases with higher densities, the increased lower component of the Dirac spinor will quench this attractive contribution. Thus we have a repulsive effect. In contrast, consider a vertex with a vector coupling, such as the one involved in the (repulsive) ω -exchange. The time component of such vertex gives

$$\bar{u}(\mathbf{p}', s') \gamma_0 u(\mathbf{p}, s) \propto \chi_s' \left(1 + \left(\frac{\boldsymbol{\sigma} \cdot \mathbf{p}}{\epsilon_p^* + m^*} \right) \left(\frac{\boldsymbol{\sigma} \cdot \mathbf{p}'}{\epsilon_p'^* + m^*} \right) \right) \chi_s , \quad (33)$$

which is enhanced as the nucleon mass decreases, resulting in additional repulsion. This argument also explains the typical relativistic enhancement of the spin-orbit force, which is mainly provided by ω exchange.

Another consequence of the larger size of the spinor lower component at higher densities is that the usual pseudoscalar (γ_5) coupling for the pion cannot be used in this context, as it would produce unreasonable results. This can be understood by noticing how the pseudoscalar vertex

$$\bar{u}(\mathbf{p}', s') i \gamma_5 u(\mathbf{p}, s) \propto \chi_s' \left(\frac{\boldsymbol{\sigma} \cdot \mathbf{p}}{\epsilon_p^* + m^*} - \frac{\boldsymbol{\sigma} \cdot \mathbf{p}'}{\epsilon_p'^* + m^*} \right) \chi_s \quad (34)$$

couples lower and upper components of the Dirac spinors. As the nucleon mass decreases (to approximately 70% of its free-space value at nuclear matter density), this contribution (and thus the entire π -exchange) grows to unreasonably large values. The pseudovector coupling of Eq. (1) does not cause these problems, which is the reason why we choose it here for the coupling of the pion to the nucleon.

This subsection has summarized the formalism for a relativistic approach to nuclear structure which is based on a relativistic extension of Brueckner theory. Relativistic meson-exchange potentials are appropriate for this framework, with the pseudovector coupling for the π NN vertex. The nucleon self-energy can be parametrized in terms of an attractive scalar and a repulsive vector field. Together with the single particle wave function, these are determined self-consistently. The attractive scalar field leads to a reduction of the nucleon mass; this effect increases with density and facilitates the prediction of nuclear saturation at the correct energy and density.

3c. Medium effects on the nuclear force

We conclude this section by demonstrating the effects of the medium (Pauli/binding and relativistic) on the nuclear force using as examples some selected partial waves.

In Figs. 1 and 2, we show the real and imaginary parts of the t - or G -matrix for some chosen S and P partial waves. In all cases, the solid curve is the free-space calculation (t -matrix), the short-dashed curve is the Brueckner-Hartree-Fock G -matrix (BHF), and the long-dashed is the relativistic G -matrix (DBHF). Plotted are half-off-shell t - or G -matrix elements as a function of momentum. At a bombarding energy of 200 MeV, the on-shell momentum is 1.55 fm^{-1} . The Fermi momentum is fixed at 1.0 fm^{-1} .

For the 1S_0 and 3S_1 partial waves in Fig. 1 and values of the momenta near the on-shell point (which are the most relevant for the processes we are considering) the t -matrix elements (solid lines) are negative. BHF medium effects are then observed to move the curves upward toward smaller absolute values. The same medium effects, when applied to the case of negative energies (that is, in nuclear matter binding energy calculations), produce repulsion. The trend is rather similar in both S -waves.

For the 3P_0 and 3P_1 partial waves in Fig. 2, BHF medium effects also move the curves upward (compare solid and short-dashed lines). In nuclear matter binding calculations [22] the medium effects on the P -waves are repulsive and generally small.

The change to a relativistically-based G -matrix calculation generally provides extra repulsion, as expected. In the S -waves, this comes primarily from the suppression of the σ -meson, as discussed in the previous subsection. For the P -waves, relativistic effects are much more dramatic. Besides the suppression from the σ , they are associated with the enhancement of the spin-orbit force, a term in the NN interaction to which the P -waves are especially sensitive.

Overall, medium effects can be large. The density dependence is shown in Fig. 3 for one case only. A proper treatment of the density-dependence of the effective NN interaction is crucial for reliable nuclear structure and reaction calculations, as we will explore in the rest of this paper.

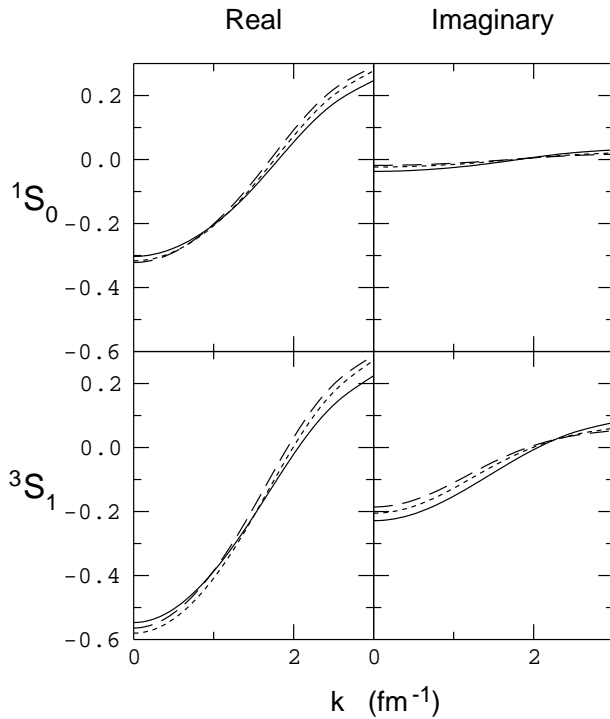


Figure 1. The real (a) and imaginary (b) parts of the half-off-shell t - or G -matrix for the 1S_0 and 3S_1 partial waves at 200 MeV. The on-shell momentum is 1.55 fm^{-1} . The solid line is the free space calculation. The short-dashed and long-dashed lines are obtained with BHF and DBHF calculations, respectively. The Fermi momentum is 1.0 fm^{-1} .

4. Transformation to an effective NN interaction

In its simplest form, the DWBA requires a perturbing potential which, for (p,p') reactions, is the NN potential described in Sect. 2. For practical calculations it has proven better to replace this with the t - or G -matrix, thereby including the full complexity of multiple meson exchange and creating what is known as the Distorted Wave Impulse Approximation (DWIA) [44]. In the case of the strong force, this also has the advantage of reducing the size of the interaction, since short-range repulsive meson exchanges tend to cancel the effects of the longer-range attractive parts. This makes the perturbation theory more tractable, since in many cases a first-order calculation suffices, and that calculation is much more accurate.

The realization of such calculations is traditionally performed by coordinate-space computer programs for which the t - or G -matrix must be transformed from momentum space to coordinate space. A popular representation for this effective NN interaction has been a series of Yukawa functions [21] which may use the same expansion for both coordinate and momentum spaces. In part, this choice is motivated by the

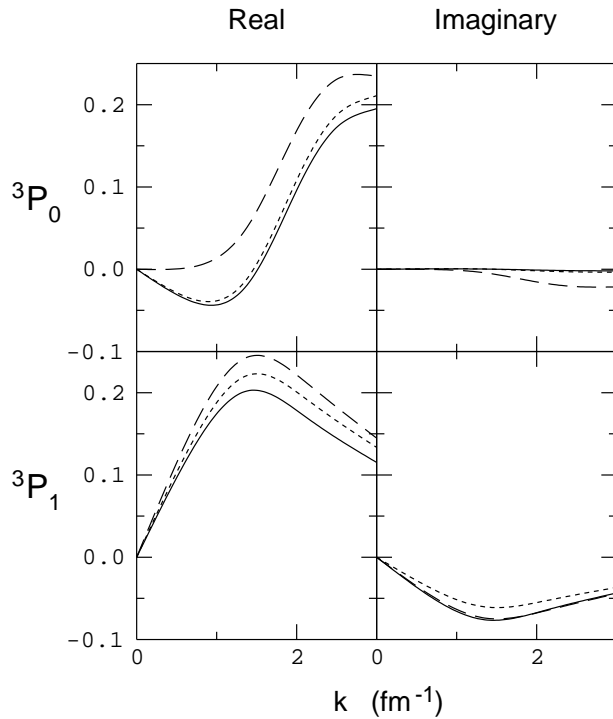


Figure 2. The same as Fig. 1 for the 3P_0 and 3P_1 partial waves.

observation that the potential in Eq. (10), $\langle \mathbf{k} | V | \mathbf{k}_0 \rangle$, is of Yukawa type and, especially for the spin-dependent parts of the interaction, is the leading contribution to the t - or G -matrix. The expansion coefficients are then obtained by making a fit of the expansion, given a pre-chosen set of ranges for the Yukawa functions, to the on-shell NN scattering amplitudes.

Some versions of coordinate-space DWIA calculations make a separation into direct and exchange parts by explicitly interchanging the indices of the projectile and struck nucleon in the exit channel. This results in a six-dimensional coordinate-space integral for the DWIA scattering matrix. A motivation for the separation is to deal explicitly with some (p,p') and (p,n) transitions in which their unnatural parity implies that there is no contribution to certain parts of the scattering matrix at zero range. Whatever contributions arise, particularly having to do with the spin dependence of the tensor parts of the interaction, are very sensitive to the distinct contributions of direct or exchange. While in our model direct and exchange are in principle distinguishable since the t - or G -matrix originates from the solution to a potential problem, historically a number of interactions were created by reproducing the amplitudes from a phase shift analysis of NN scattering where such a distinction is not possible. So in this expansion it was assumed that the sum over Yukawa functions was the direct part, and the full NN scattering amplitude was generated using the

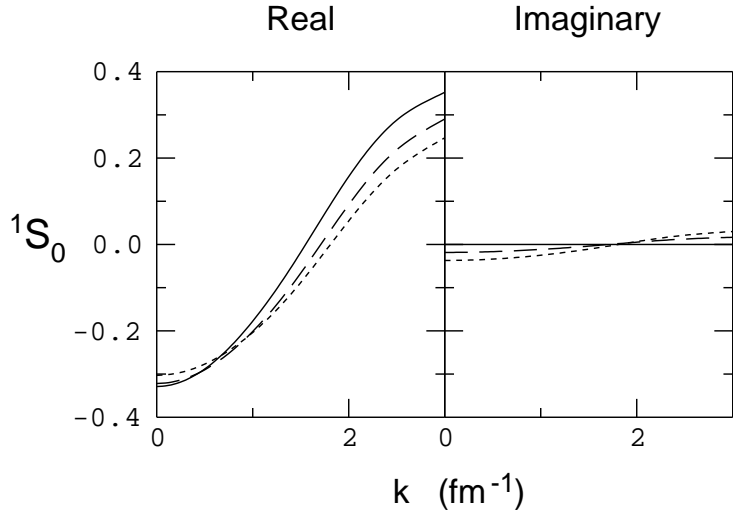


Figure 3. Density dependence of the 1S_0 half-off-shell partial wave amplitude at 200 MeV. The solid curve is for $k_F = 0 \text{ fm}^{-1}$, the short-dashed for $k_F = 1.0 \text{ fm}^{-1}$, and the long-dashed for $k_F = 1.35 \text{ fm}^{-1}$.

symmetries of NN scattering [21]. In effect, this leads to a different set of functions that are fit to the NN amplitudes. The hope is that this artificial separation will then work in a practical calculation.

There are a number of reasons to expect that this approximation is actually satisfactory. For the central and spin-orbit parts of the effective NN interaction, the spin operator for the direct and exchange amplitudes is the same. So in the end, these two pieces are added together again just as they were when the original fit was made to the NN scattering amplitude. The quality of this approximation is enhanced since the central parts are usually largest at zero range where the distinction between these two pieces disappears. For the tensor terms, it is known that the direct piece has to depart from zero momentum transfer as q^2 , so any NN amplitude near $q = 0$ must be part of the exchange piece. Also, the parts of the interaction associated with the $S_{12}(\hat{q})$ and $S_{12}(\hat{Q})$ spin operators [$\hat{\mathbf{q}} = (\mathbf{k}' - \mathbf{k})/|\mathbf{k}' - \mathbf{k}|$, $\hat{\mathbf{n}} = (\mathbf{k} \times \mathbf{k}')/|\mathbf{k} \times \mathbf{k}'|$, and $\hat{\mathbf{Q}} = \hat{\mathbf{q}} \times \hat{\mathbf{n}}$] arise essentially from the interplay of the real potentials from π - and ρ -meson exchange with little contribution from the integral of Eq. (10). Thus, if the Yukawa functions simulate well the real parts of the π - and ρ -meson exchanges, other parts of the tensor interaction will fall into place. Since our long-term purpose is to bring together diverse sources of information about the NN interaction, it was decided that we would continue to make the separation between direct and exchange in this model-dependent way.

These observations are also useful in assessing where we expect there to be large density-dependent effects. Since most of the density dependence in Eq. (10) enters through the integral, (this is exactly true for BHF effects, which only enter the picture in second or higher order), terms in the effective NN interaction

where $\langle \mathbf{k} | G(\mathbf{P}, k_F) | \mathbf{k}_0 \rangle \approx \langle \mathbf{k} | V | \mathbf{k}_0 \rangle$ will be relatively free of these effects. This applies to the tensor parts of the interaction. In fact, the largest differences arise for the isoscalar central and spin-orbit parts of the effective NN interaction, and these are the parts that drive the excitation of the natural parity states we will study. Since $\langle \mathbf{k} | V | \mathbf{k}_0 \rangle$ is real, the imaginary parts of the effective NN interaction all arise from the density-dependent integral, and would be expected to manifest the effects of the nuclear medium to the extent that they make large contributions to the total transition amplitude for their particular spin operator.

The various amplitudes for the effective NN interaction are separated among the five spin operators according to

$$t = t_0 + t_\sigma \sigma_1 \cdot \sigma_2 + t_S (\sigma_1 + \sigma_2) \cdot n + t_{TD} S_{12}(\hat{q}) + t_{TX} S_{12}(\hat{Q}) . \quad (35)$$

The five pieces in order are the central, spin-spin, spin-orbit, tensor direct, and tensor exchange. Each amplitude is divided into two pieces that correspond to the isospin operators $\mathbf{1}$ and $\tau_1 \cdot \tau_2$. There are then 10 complex amplitudes all together. Each piece is represented for the direct part by a sum of from 2 to 4 Yukawa functions.

The coefficients for each Yukawa function in each sum are determined so as to best reproduce the NN amplitudes. From the G-matrix calculation, there are complex values of the G-matrix elements. These form an array whose index consists of the partial wave quantum numbers. Likewise the Yukawa coefficients can be put into an array, and there is a linear transformation that connects the two. For this transformation, we actually convert the G-matrix elements into the corresponding S-matrix representation. The transformation, discussed more fully in the Appendix, is then the matrix \mathbf{M} in $\mathbf{S} = \mathbf{M}\mathbf{V}$ where \mathbf{S} is a vector composed of the S-matrix elements and \mathbf{V} is a vector of Yukawa coefficients. Because of the long range of the pion tail, it is useful to extend the range of S-matrix elements up through $J = 15$. In this case there are more partial waves than Yukawa coefficients, and a fit is necessary. Since the system is linear, this can be accomplished in one step. Using dS_i as the error on any particular S-matrix element (set here to the same value for all partial waves), we can define the vector and matrix

$$\mathcal{S}_j = \sum_i \frac{S_i M_{ij}}{dS_i^2} \quad \mathcal{M}_{jk} = \sum_i \frac{M_{ik} M_{ij}}{dS_i^2} \quad (36)$$

from which the solution for the Yukawa coefficients is simply

$$V_k = \sum_j \mathcal{M}_{jk}^{-1} \mathcal{S}_j . \quad (37)$$

For our work near 200 MeV, we chose the ranges used by Franey and Love [45] at 210 MeV and found satisfactory results for all nuclear densities.

Once the transform matrix \mathbf{M} is available, it may be used to go from the Yukawa coefficients back to the NN G-matrix elements. It is also possible to compare the effective NN interaction, for example as a function of momentum transfer, with the corresponding NN scattering amplitudes. So a number of checks of this transformation are possible. For the polarization observables, the differences are in all cases well within

0.01, so the quality of this fit is not an issue for subsequent comparisons. It is, in fact, somewhat remarkable that such a high quality of fit is available with so few terms in the Yukawa expansion for each part. The spin-orbit, for example, contains only two for each of the real and imaginary parts. This is, perhaps, further support for the use of Yukawa functions as the direct part of the effective NN interaction.

This transformation is similar to that used by Karataglidis *et al.* [46] to provide an effective NN interaction for their study of $^{12}\text{C}(p,p')$ reactions. In their case, they also consider the off-shell parts of the G-matrix within about 0.5 fm^{-1} of the on-shell point. We have used their formulation, and do not find that this added sensitivity significantly changes the (p,p') calculations. So we have not incorporated that extension into the work here.

5. The DWIA calculations

In the longer term, we wish to use the techniques set forth here to examine the question of medium modifications for a large body of polarization transfer data taken at 200 MeV. Here, we evaluate the calculations at this energy using (p,p') measurements where the conventional medium effects are expected to be large and where the theory could be capable of describing the data. For this purpose, we have chosen natural parity transitions measured in ^{16}O and ^{40}Ca at 200 MeV [29], and in ^{28}Si at 180 MeV [30]. In the original work where these data were first reported, measurements of the cross section and analyzing power were matched with a phenomenological effective NN interaction using the DWIA program LEA [23]. We have obtained a copy of this program and have used it in a manner modelled after the applications described by Seifert and Chen.

LEA makes use of a pseudopotential form of the Born approximation in which each term of the effective NN interaction is folded with the appropriate piece (depending on spin operator coupling) of the nuclear density. The resulting effective potential is then used to calculate the transition amplitudes by overlapping it with a distorted wave description of the projectile motion and the appropriate piece of the transition density. This scheme uses a system in which the spatial coordinate is tied to the position of the projectile. Thus it is most appropriate for the calculation of the direct part of the scattering. Exchange is handled in a zero range approximation that adds this piece of the effective NN interaction to the direct part, and the overlap is calculated as it would be if the outgoing nucleon were the projectile. For all prior work with LEA [29,30], the exchange part of the effective NN interaction has been calculated at a momentum transfer of zero, then added to the direct part. It is thus a constant, independent of momentum transfer.

In the investigation of the high spin states of ^{28}Si , we modified this treatment of exchange to allow the exchange momentum transfer Q to vary with the momentum transfer q [20]. The incoming and outgoing proton momenta were constrained to their laboratory values. This means that for a given scattering angle, the outgoing momentum from a particular state will be different than it would be if the scattering took place from a nucleon in free space. To make this scattering happen with on-shell kinematics, it is necessary to have

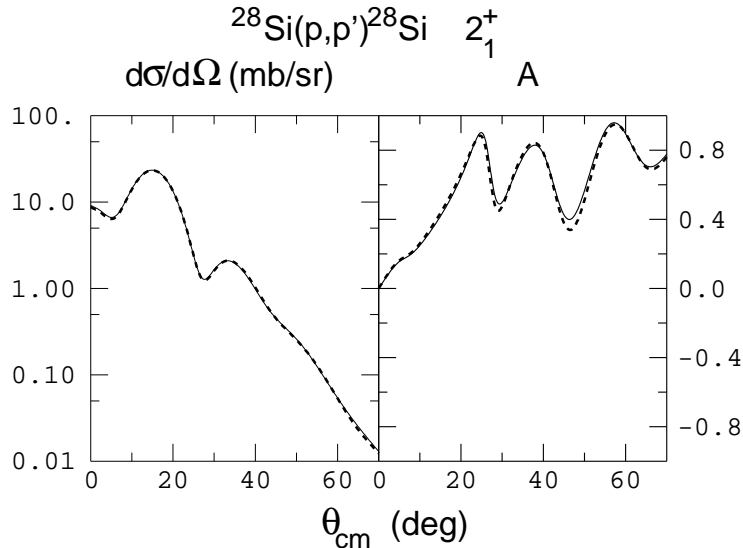


Figure 4. Calculations of the cross section and analyzing power for the first 2^+ state in ^{28}Si . The thin solid curves use the zero range prescription of LEA [23], the heavy dashed curves use the formulation described in the text.

the struck nucleon in motion prior to the collision. There are an infinite number of solutions to this problem. We chose the one with the smallest possible momentum for the struck nucleon relative to the center-of-mass motion of the target nucleus, with the idea that the momentum-space wavefunction for the bound nucleons falls off as a function of momentum and that the typical value would be close to this limit. This permits the calculation, as a function of scattering angle, of both the momentum transfer q and the exchange momentum transfer Q , taking the latter to be the change in momentum when the struck nucleon is the detected nucleon. In Fig. 4 we compare two calculations for the $^{28}\text{Si}(p,p')^{28}\text{Si}$ reaction to the first 2^+ state. The solid curve uses the original zero range approximation [$Q(q) = Q(q = 0)$] of LEA, and the heavy dashed line is based on the functional values of $Q(q)$ just described. The curves are essentially indistinguishable. So while this choice is important for the treatment of the exchange tensor parts of the effective NN interaction, it is not a serious issue here.

In other aspects, our calculations with the DWIA program LEA followed the scheme described by Seifert [29] and Chen [30]. The entrance and exit channel distortions were calculated using a first-order folding prescription ($t\rho$). The same density-dependent interaction is used for both the elastic and inelastic calculations except for the small change to the exchange part required by the different reaction Q-value. However, there are corrections to the density-dependence that are different between the elastic and the inelastic channels [47,48], and these have been included. In addition, there is a small downward rescaling of the effective NN interaction that has to do with the change between the nucleon-nucleon and the nucleon-

nucleus frames of reference [49,21], and this has also been included.

The ground state nuclear matter density is needed to determine the density at which the interaction should be evaluated. We have taken the longitudinal formfactor for elastic electron scattering [50] and corrected it for the charge distribution of the proton using an unfolding procedure available in LEA. What remains from the deconvolution is assumed to be a point nucleon density that applies to both protons and neutrons, since all of the targets considered here have equal proton and neutron numbers. This density is then evaluated at the position of the projectile. No alterations are made to account for different densities at the position of the struck nucleon. This “local density approximation” is similar to the zero range approximation for the exchange part of the interaction, in that both assume that the strongest part of the transition takes place when the projectile and struck nucleons overlap.

The transition formfactors have been calculated by Seifert [29] and Chen [30] in a series expansion based again on longitudinal electron scattering measurements. We use their expansions here.

6. Variations within the Effective Mass Ansatz and their Impact

For both the BHF and DBHF treatments of the in-medium interaction, the exact nuclear matter potential $U(p)$ of Eqs. (15) or (30) is approximated by an analytical function containing the kinetic energy term and a constant [see Eqs. (17) and (31)]. This approximation facilitates later developments in the self-consistent procedure [5]. The two adjustable coefficients are usually obtained by matching the approximating function to the exact $U(p)$ at two values of p . For nuclear matter calculations, where all momenta are below k_F , the usual procedure [22] is to match at $p = 0.7k_F$ and k_F . To illustrate the quality of this approximation, the solid curve in Fig. 5 shows the exact DBHF potential of Eq. (30) for $k_F = 1.35 \text{ fm}^{-1}$. The approximating function matched at low values of p is shown by the long dashed curve. When considering scattering by nucleons in the continuum, much higher momenta are involved, and we see from Fig. 5 that the long dashed curve becomes a poor approximation for high momenta. The laboratory beam momentum at 200 MeV is 3.2 fm^{-1} , and is shown by the arrow in Fig. 5. The approximation can be improved in the vicinity of the beam momentum by matching the approximating function at higher momenta. We have chosen $2k_F$ and $4k_F$, which spans the range of momenta covered here. This choice gives rise to the short dashed curve, which is seen to rise more gradually with p , and thus correspond to a larger (and closer to the free value) effective nucleon mass.

Figure 6 shows the effective nucleon mass as a function of the Fermi momentum for the cases we have just described, namely BHF or DBHF for both low or high matching momenta. For either matching criterion, the BHF and DBHF masses are close to each other, with the DBHF masses being slightly smaller. The DBHF high momentum match was checked and still found to be consistent with the saturation properties of nuclear matter. (We obtained saturation at $0.17 \text{ nucleons/fm}^3$ with a binding energy of 14.4 MeV.)

It is useful to compare the impact of each of these G-matrix schemes on the effective NN interaction.

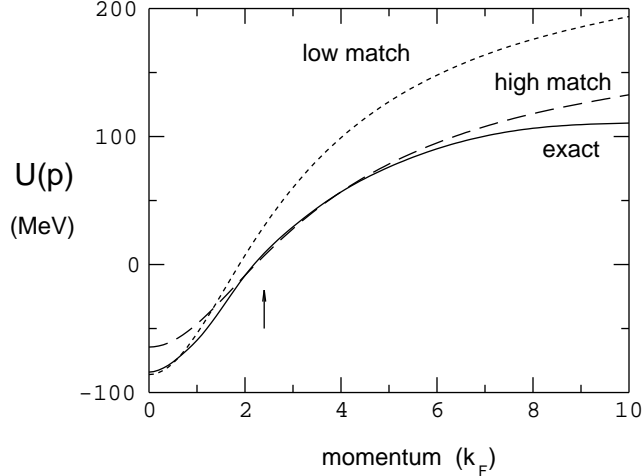


Figure 5. The momentum dependence of the exact (DBHF) in-medium NN potential $U(p)$ at $k_F = 1.35 \text{ fm}^{-1}$ (solid). The two approximate potentials are matched at low momentum (long dash) and high momentum (short dash). The arrow marks the beam momentum corresponding to a laboratory energy of 200 MeV.

For this we have chosen the central, isoscalar, spin-independent interaction at $q = 0$ [first term in Eq. (35)]. The real part is shown in the left and center panels of Fig. 7 for the four cases just discussed. The difference between DBHF and BHF is here much more dramatic than is apparent from the values of the effective nucleon mass, primarily because the effective mass in DBHF also alters the strength of the terms in the OBE potential. For the standard BHF treatment, these terms remain unchanged with changing nuclear density. Clearly, choosing the higher matching momenta reduces the size of both effects. The imaginary part of the same effective NN interaction term (not shown here) is negative in all cases, and becomes weaker as the density increases. Also, there is much less variation among the different cases.

The size of the interactions shown in Fig. 7 will also have an effect when used in a folding model to produce an optical potential for Distorted Wave calculations. Given a point nucleon density distribution for a nucleus, this model averages the interaction across the nucleus for each radial point in the optical potential. Values of the interaction term shown in Fig. 7 for low density contribute to an attractive real central optical potential, and this will be typical of the folded optical potential in the low-density region of the nuclear surface. As the local density increases, the stronger medium effects associated with the DBHF G-matrix will push the optical potential positive. The ^{40}Ca optical potentials for 200 MeV corresponding to some of the curves of Fig. 7 are shown in Fig. 8, and the resulting predictions for differential cross section and analyzing power are compared to elastic scattering data on ^{40}Ca [29] in Fig. 9.

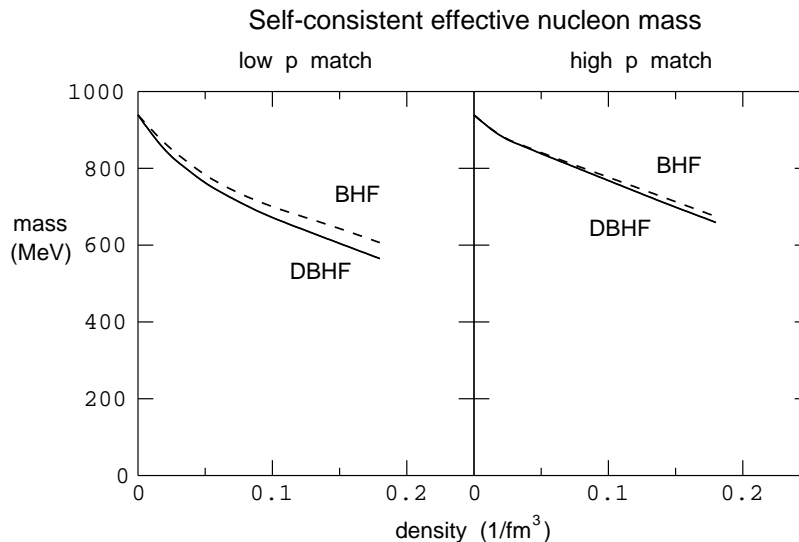


Figure 6. The effective nucleon mass as a function of k_F . The left and right panels show the masses obtained using low and high matching points as explained in the text. The values for BHF (dashed) and DBHF (solid) are marked.

In comparing potentials, it is important to realize that the most important region is near the nuclear surface from 3 to 5 fm. The free case (duplicated for left and center panels) uses only the free space interaction, and produces a potential that is too attractive. This attraction tends to draw elastic scattering flux into the nucleus where the spin-orbit potential becomes more efficient at separating spin up and down components in the proton beam. This produces an analyzing power that is too positive. Obtaining the right amount of surface attraction, and the right average value for the analyzing power, then becomes one important criterion for evaluating the folded optical potential.

It is interesting to observe that the BHF calculation with low momentum matching points is free of these problems. In fact, as can be seen in the lower left panel of Fig. 9, the dashed curve represents an excellent prediction for the analyzing power. While too large at angles past 30° , the cross section in the upper left panel of Fig. 9 is also an improvement. The success of this model has been noted on many occasions, and much effort has gone into a microscopic treatment of elastic scattering [51–56] and its extension into a momentum space representation [57–59]. For lower mass target, the small rise in the BHF optical potential near 3 fm grows until it is near 0 MeV. This produced in the early 1980’s work on the “double humped” potential for ^{12}C [60]. Angular distributions at very large scattering angles tended to confirm this prediction in phenomenological potential shapes. At the same time, the imaginary part of the free interaction was too absorptive. Moving to a BHF treatment cut the size of this almost in half, which was important in obtaining consistency with other calculations of the mean free path of protons in nuclei [61,62].

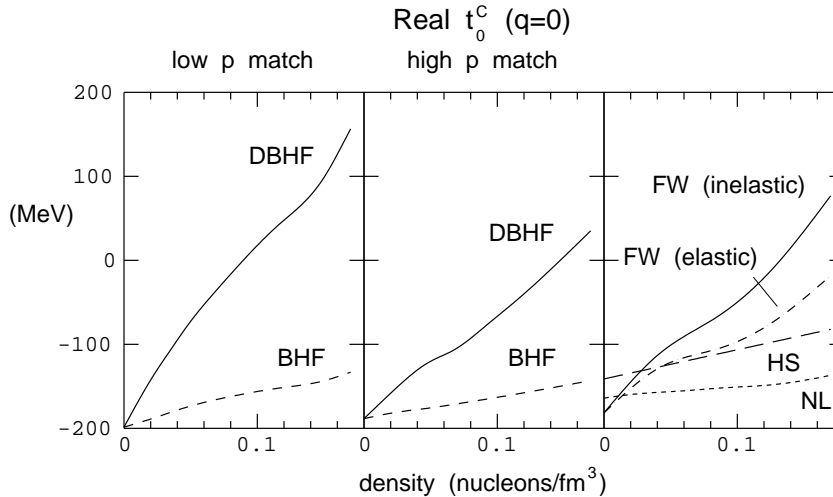


Figure 7. Variation with nuclear density of the real isoscalar, central, spin-independent effective NN interaction at $q = 0$. The left and center panels repeat the cases of Fig. 6. The right panel includes cases from the literature: Furnstahl-Wallace for inelastic and elastic channels [28], Nakayama and Love [26], and the empirical effective NN interaction of H. Seifert [29].

It is interesting to note in passing that the same time produced a number of studies of elastic proton scattering based on the Dirac equation and large scalar and vector optical potentials. These also did well in reproducing data, and when reduced to a Schrödinger form potential as in Fig. 8, a “double hump” form was also produced. Thus there appeared to be two explanations of the same phenomenological result.

Returning to our G-matrix schemes, from the left panels of both Fig. 8 and 9 it would appear natural to conclude that the DBHF calculation overestimates medium effects, while BHF produces a more reasonable description of both cross section and analyzing power. On the other hand, moving to the center panel (high momentum match) shows that the DBHF predictions improve noticeably. Thus different choices within the effective mass approximation seem to have considerable impact on the size of the medium effects, which will be reflected on the distorting potential and scattering observables.

At this point the results of Furnstahl and Wallace [28] are instructive. They start from an OBE potential that is fully relativistic [63], and solve the Dirac equation in the nucleus. They also include Pauli blocking and nuclear binding effects. The interactions from their work suitable for elastic and inelastic scattering are shown, together with others, in the right panels of Figs. 7-9. We notice that the inelastic interaction of Furnstahl and Wallace has the same problem as our DBHF when compared with the elastic scattering data, namely a cross section that is too large at large scattering angles and an analyzing power that is too negative.

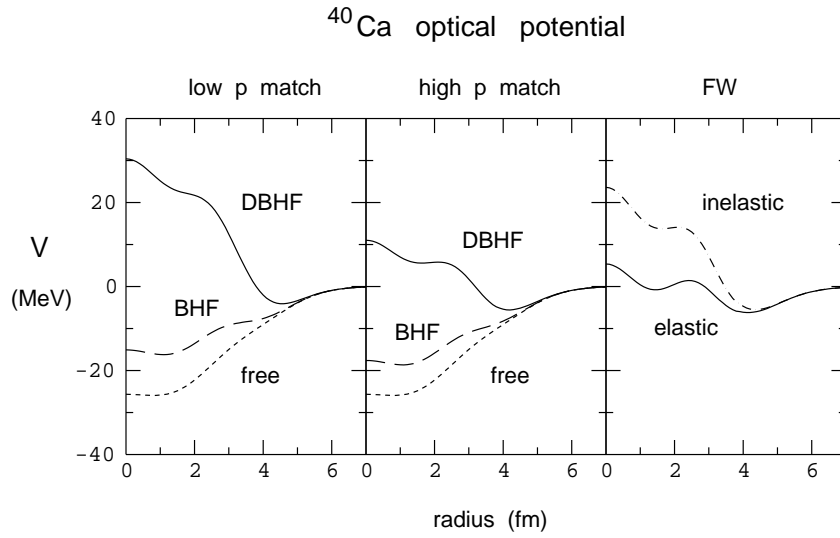


Figure 8. Real central potentials calculated using the folding model for ^{40}Ca at 200 MeV for some of the interactions of Fig. 7.

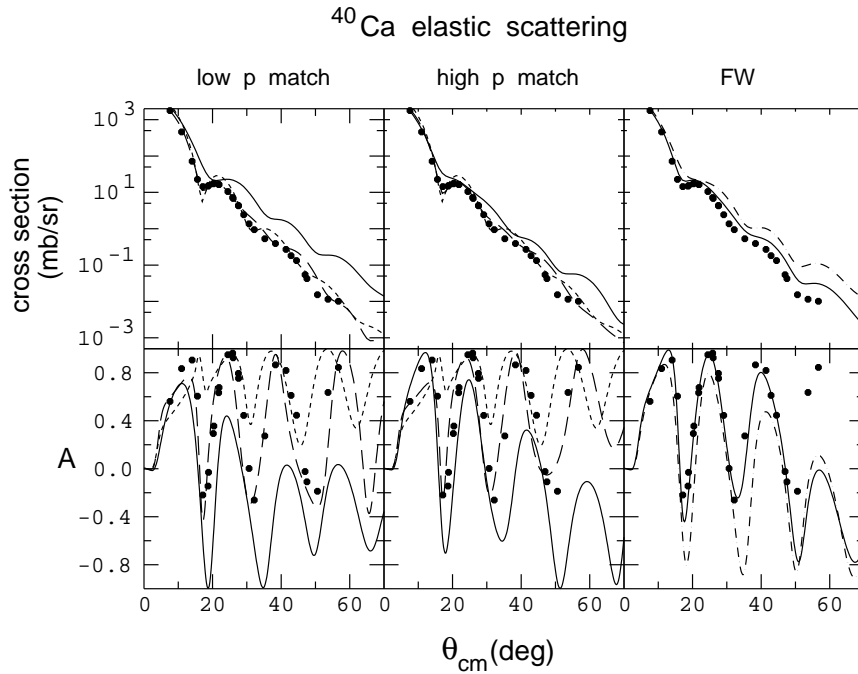


Figure 9. Elastic scattering cross section and analyzing power measurements for ^{40}Ca at 200 MeV. The calculations use the optical potentials of Fig. 8.

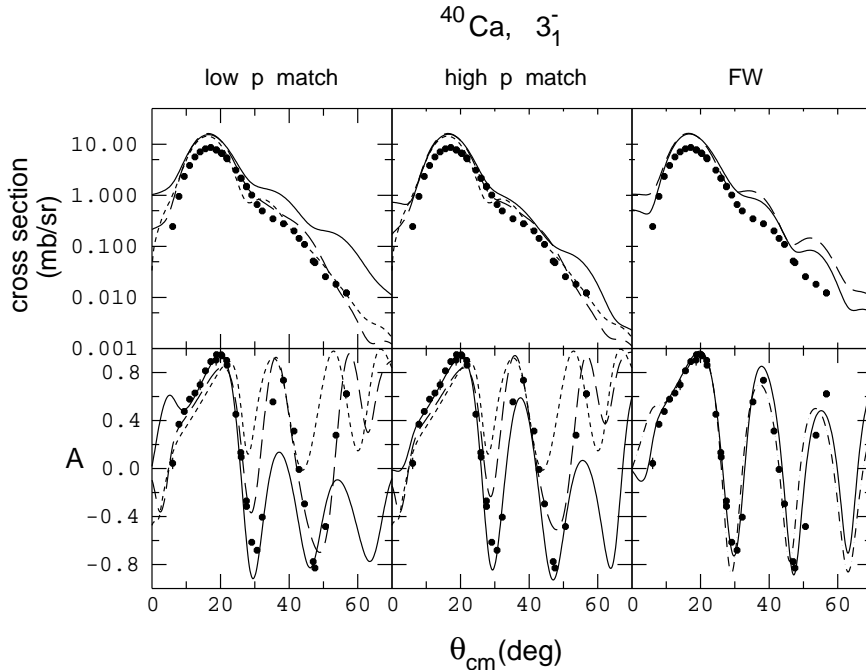


Figure 10. Measurements of the cross section and analyzing power for the first 3^- state in ^{40}Ca . The curves are described in Fig. 7

By treating finite nuclear systems, Furnsthal and Wallace point out that in the elastic scattering channel, the identity between the entrance and exit channels removes one power of the Möller operator, thus significantly reducing the relativistic effects. These calculations are shown by the solid lines in the right hand panels of Figs. 7-9. For this case, both cross section and analyzing power are in better agreement, though their behaviour at large scattering angles suggests that medium effects in this model are still too large, an observation that echoes their comparison to (p,p') measurements [64].

The above comparison suggests that a reduction in the Dirac effects of our model by about the size of the Möller operator change in Furnsthal and Wallace would be likely to improve the agreement with the elastic scattering data. Thus the ingredients described here would appear to be adequate to understand proton elastic scattering within a G-matrix approach that also reproduces the density and binding energy of nuclear matter.

Since the primary focus of this paper is to establish a reliable basis for inelastic scattering calculations, it is important to examine the implications for this process of the model variations described above. In Fig. 10 we present calculations for the $^{40}\text{Ca}(p,p')^{40}\text{Ca}$ reaction to the 3^- state at 3.736 MeV. For the left and center panels, the same interaction is used to generate both the folding model optical potential and the inelastic transition. The curves follow the same scheme as Figs. 7-9. Again, switching to high momentum matching reduces the density-dependent effects. Then the DBHF predictions appear to be the best, and we will use this scheme in the rest of this paper. The right panels show the Furnstahl and Wallace result. Here

the dash-dot curve substitutes the inelastic interaction in the calculation of the folding model distortions. The good agreement with the DBHF (high momentum match) scheme and the small difference between the two Furnstahl results would suggest that using the correct inelastic interaction is more important than the Möller operator change to the distortions. Thus the DBHF scheme (together with the approximation illustrated by the short-dashed curve in Fig. 5) is a reasonable one.

7. Results of the DWIA Calculations

After discussing the sensitivity of the predictions to some of the model ingredients, in this section we will present and discuss the results from the DBHF model interaction (with the larger effective masses shown in the right panel of Fig. 6). We will begin with some additional comments about the calculation of elastic scattering, then move to comments concerning the choice of the OBE potential and some observations concerning a variety of natural parity transitions in ^{16}O and ^{40}Ca at 200 MeV, and in ^{28}Si at 180 MeV.

Figure 11 shows the folding model calculations for proton elastic scattering from ^{16}O and ^{28}Si using the free (short dash), BHF (long dash), and DBHF (solid) interactions. These curves were calculated in the same manner as the curves in the center panels of Fig. 9 for ^{40}Ca . The local nuclear matter density was derived from the longitudinal electron scattering form factor [50], as described in sect. 5. All of these measurements are at 200 MeV. The data for ^{28}Si were taken in connection with an investigation of high spin states in that nucleus [20]. The features here are similar to those described for ^{40}Ca in the previous section. The DBHF calculations in their present form overestimate the cross section and predict values for the analyzing power that are generally too negative. In the analyzing power, we see a progression from positive to negative values as the size of the density dependence increases. This suggests that the total density dependence is too large, an effect that may be associated with the infinite nuclear matter assumption of our G-matrix calculation.

It is clearly possible to achieve a better phenomenological description of the elastic scattering measurements through the use of optical potentials with adjustable shapes. Such a calculation [65] for proton elastic scattering on ^{28}Si at 180 MeV is shown by the dashed line in Fig. 12. The parameters of this potential vary smoothly from 80 MeV [65] up to 200 MeV [66]. Clearly the adjusted optical potential produces a good fit to the data, but it is valid to ask whether the optimization of the fit to the elastic data builds in any prejudice. As is the case with most optical model work, measurements are missing at small angles where the cross sections are largest. Thus the adjustment weighs more heavily the larger angle data where the cross section has fallen a few orders of magnitude and coupling to the major reaction channels may already be important.

One way to address this issue is to compare the two approaches to the distorted wave calculations for (p,p') transitions. Fig. 13 shows two DBHF calculations for the $^{28}\text{Si}(p,p')^{28}\text{Si}$ reaction to the 2^+ state at 1.779 MeV. The bombarding energy is 180 MeV and the form factor comes from the work of Chen [30]. The solid curves employ folding model distortions, while the dashed curves are based on the best-fit

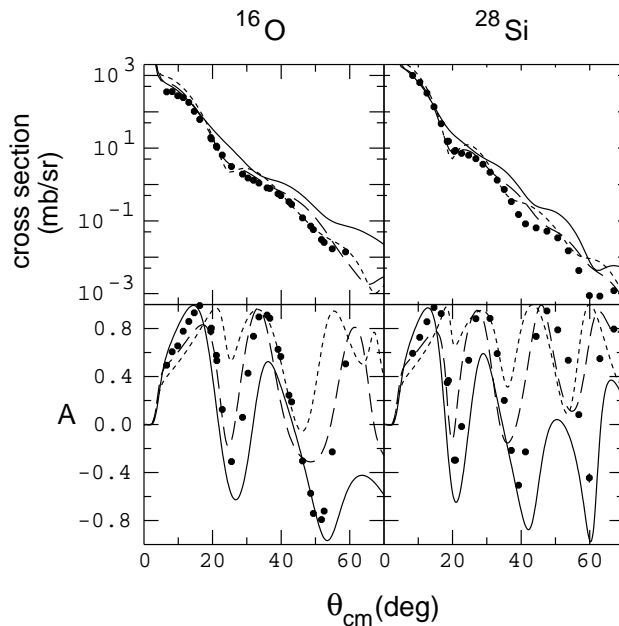


Figure 11. Measurements of the cross section and analyzing power for ^{16}O and ^{28}Si at 200 MeV. The folding model calculations are based on the free (short dash), BHF (long dash), and DBHF (solid) forms of the effective interaction.

phenomenological potential from Olmer [65]. The analyzing power and cross section angular distributions both favor the use of folding model distortions. The best-fit optical potential gives cross section predictions that fall too slowly at the larger angle. For the analyzing power, both calculations do equally well in locating the diffraction pattern in angle, but the analyzing power predicted with the best-fit optical potential is too positive. The same issues are also present for the other strong (p,p') transitions included in this study. Thus we are better served by using distortions calculated within the folding model, despite the concerns presented in the previous section.

Another point to realize is that with the measurement of a number of very precise NN polarization observables near 200 MeV [67], the quality of the OBE potential has improved. Because of the much larger theoretical uncertainties introduced by the G-matrix calculations, it is not practical to evaluate this issue by a direct comparison with (p,p') data. Instead, in Fig. 14 we show two calculations for the $^{40}\text{Ca}(p,p')^{40}\text{Ca}$ reaction to the 3^- state at 3.736 MeV based on this work and the similar but earlier Bonn-B interaction [22]. For simplicity, neither calculation contains density dependence. There are differences between the solid curve (Bonn-B) and the dashed curve (the OBE presented here), particularly for the analyzing power. On the scale of our comparison to (p,p') data such differences matter, especially since they are systematic across all transitions. Similar problems arise for other popular interactions, such as the density-dependent interactions of von Geramb [24,25] and Nakayama [26], as well as other free interactions such as the one from the Paris group [68]. As discussed previously [69], most modern interactions [70,34] are based on the

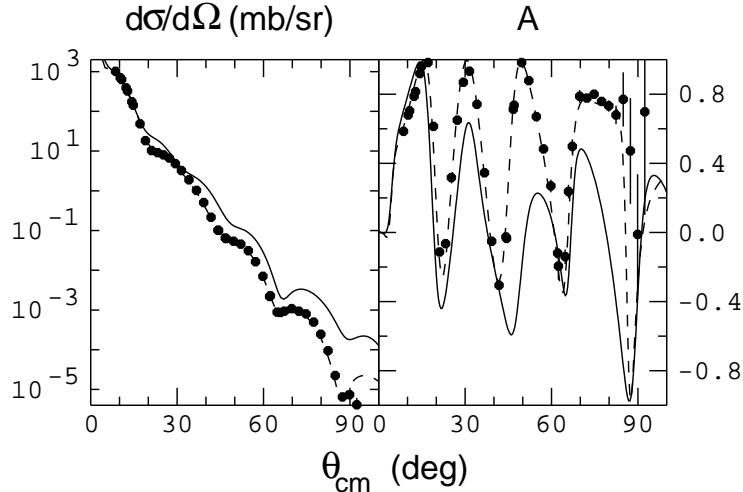


Figure 12. Measurements of the cross section and analyzing power for proton elastic scattering on ^{28}Si at 180 MeV. The solid curves show the results of a folding model calculation; the long dashed curves are the final values from a phenomenological optical potential fit to these data [57].

NN data base and phase shift analysis of the Nijmegen group [33] and are correct to the extent that their selection of the NN data to be considered is appropriate. In general, the older interactions are not as faithful to the present NN scattering data, especially for measurements involving polarization, and are likely to have larger discrepancies when compared to (p,p') measurements.

Lastly, we will present calculations for a number of natural-parity transitions in ^{16}O , ^{28}Si , and ^{40}Ca in order to illustrate some additional properties and issues associated with our model.

Figure 15 contains three strong collective states not previously shown here,

along with calculations using the free (short dash), BHF (long dash), and DBHF (solid) effective interactions. Presentation of all three interactions again illustrates the effect of the major density-dependent contributions. In all cases the peak of the cross section is overpredicted by about 50%. A number of factors have been included that reduce the cross section, including relativistic kinematics for the transformation from t-matrix to the Yukawa expansion, and the transformation of the interaction from NN to N-nucleus coordinates described by Eq. (14) of Love and Franey [21]. This has been an issue in other investigations, and has been handled in the empirical interaction of the Kelly group [29,30] by attenuating the free interaction by factors of about 0.8. This appears in Fig. 7 as a less negative value of the Seifert central interaction at $k_F=0 \text{ fm}^{-1}$ (the slope is then adjusted to best match the same body of (p,p') transitions that we consider here). There the overestimate has been ascribed to an inadequacy in the local density approximation in

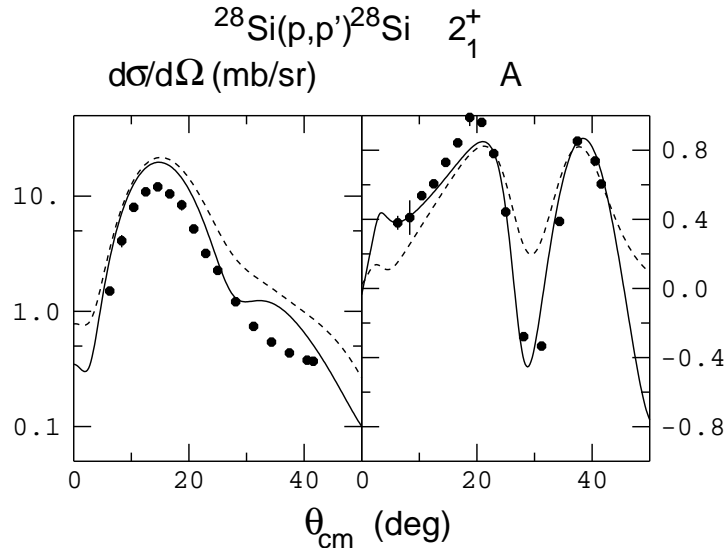


Figure 13. Measurements of the cross section and analyzing power for the $^{28}\text{Si}(p,p')^{28}\text{Si}$ reaction to the 2^+ state at 1.779 MeV. The DBHF calculations are based on folding model (solid) and phenomenological best-fit optical potentials (dashed).

which the density dependence is scaled to the nuclear density at the coordinate of the projectile rather than considering some average over the locally changing density that lies within the range of the NN interaction. At lower bombarding energies such overestimates of the cross section in DWBA calculations have been attributed to distorted wave functions that are too large in the nuclear interior because they ignore exchange non-localities [71]. Inclusion of the standard correction (scaled to the energy dependence of the strength of the central optical model potential) in fact increases the cross section at the peak and does not, at least in this form, represent a helpful way to handle this issue.

Generally, the shapes of the cross section angular distributions match the data well. Of the three calculations shown, the best reproduction of the analyzing power is clearly with the DBHF predictions. Thus a model that is consistent with the bulk properties of nuclear matter is also best for nucleon-induced reactions.

For the weaker (p,p') transitions, agreement with the calculations is a bit more elusive. In Fig. 16, we again show the three types of calculations for the 0^+ state in ^{28}Si at 4.98 MeV and the 1^- state in ^{16}O at 7.117 MeV, both non-collective transitions of low spin. For the most part, the general features of the cross sections are reproduced, as would be expected since the transitions form factors are taken from (e,e') data.

The higher spin states shown in Fig. 17 have simpler angular distributions. Here the quality of the reproduction is comparable to the strong collective states shown in Fig. 15. All of the analyzing powers show

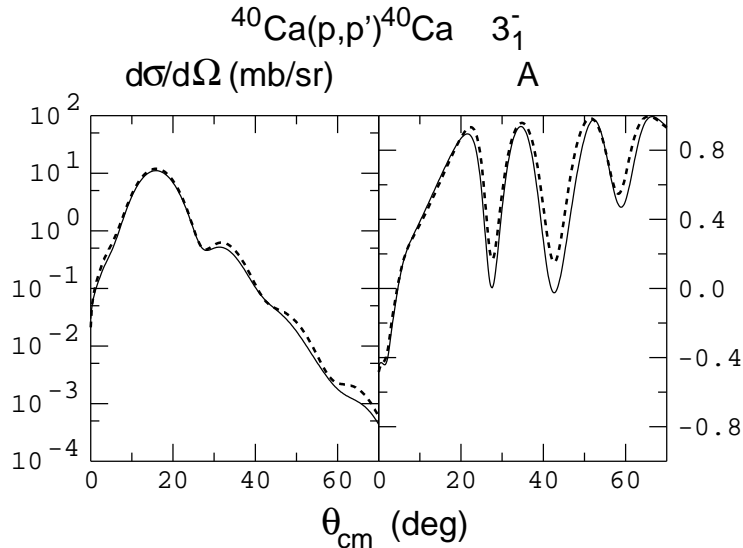


Figure 14. A comparison of two free interaction calculations for the $^{40}\text{Ca}(p,p')^{40}\text{Ca}$ reaction to the 3^- state at 3.736 MeV. The solid line uses the Bonn-B interaction and the dashed line uses the OBE potential of sect. 2.

a falling angular distribution between 20° and 40° that is well reproduced and shows little effect from the density dependence. The overestimate of the cross section near the peak is still present.

None of the results so far discussed bear on the question of whether the density dependence is correct, regardless of questions about the size of the interaction. For this we need states whose transition densities peak at nuclear densities that are sufficiently different to make a meaningful comparison. This opportunity is present for ^{28}Si , where the series of 2^+ states shows the needed variety. In Fig. 18, the states considered in this analysis (cleanly resolved in the experiment) are shown in order of decreasing reaction radius. This change is apparent from the expansion of the diffraction pattern as the reaction radius goes down. If the reaction radius is larger, then one would expect that most of the transition takes place in regions of the nucleus where the density is small and that changes to the effective NN interaction would be modest. This appears to be the case, as the size of the density-dependent modifications increases going from left to right in Fig. 18. This is true of both the cross section and the analyzing power. For the first state (4^{th} in excitation) all calculations do a reasonable job capturing the features of the analyzing power angular distribution. As the radius moves the transition to regions of higher nuclear density, the DBHF calculations continue to follow the measurements. So the changing amount of density dependence needed to describe this series of transitions is captured by our model.

In closing this section, we observe that a quantitative, relativistic two-body force, combined with a Dirac approach to nuclear matter, provides a good description of the main features of the (p,p') data considered

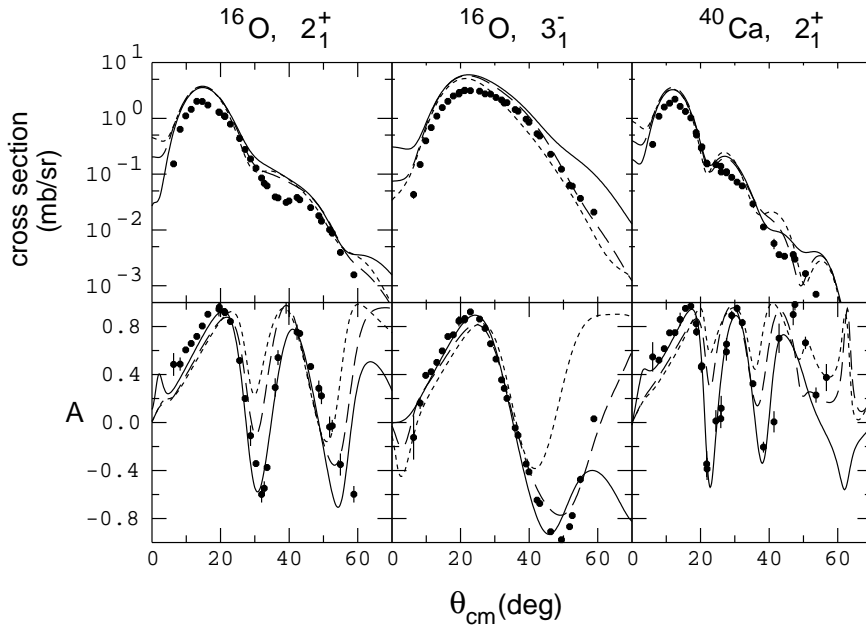


Figure 15. Measurements of the cross section and analyzing power for the (p,p') reaction leading to the 2^+ and 3^- states in ^{16}O at 6.917 and 6.130 MeV and the 2^+ state in ^{40}Ca at 3.904 MeV. The curves are based on the free (short dash), BHF (long dash), and DBHF (solid) interactions.

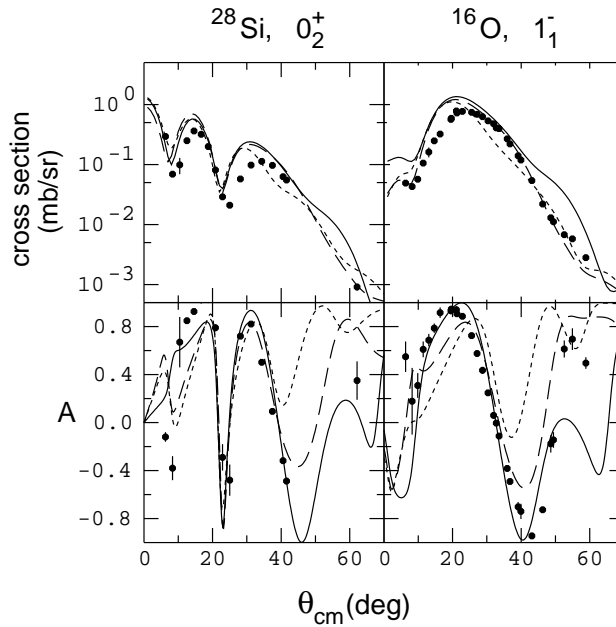


Figure 16. Measurements of the cross section and analyzing power for the 0^+ state in ^{28}Si at 4.98 MeV and the 1^- state in ^{16}O at 7.117 MeV, along with calculations as described in Fig. 15.

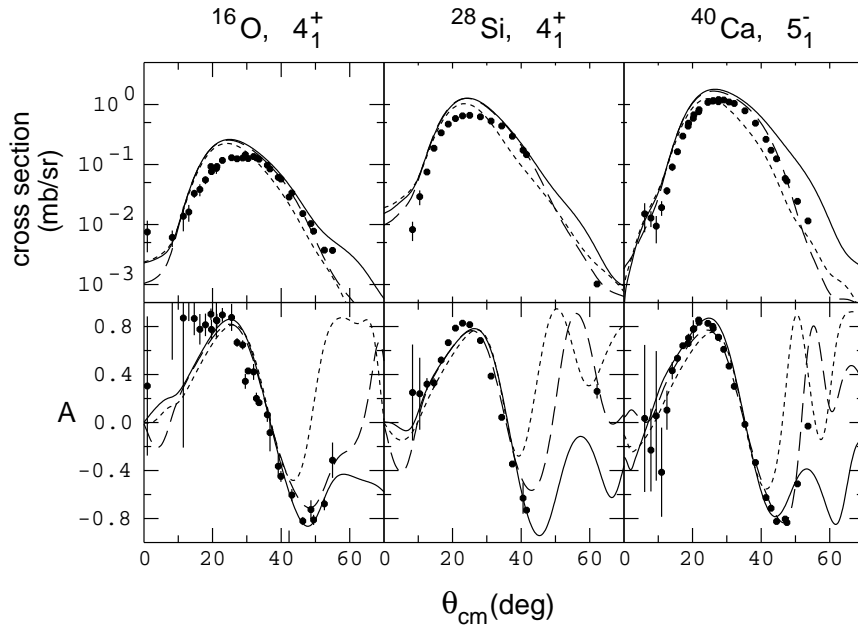


Figure 17. Measurements of the cross section and analyzing power for the 4^+ state in ^{16}O at 10.356 MeV, the 4^+ state in ^{28}Si at 4.62 MeV, and the 5^- in ^{40}Ca at 4.492 MeV, along with calculations as described in Fig. 15.

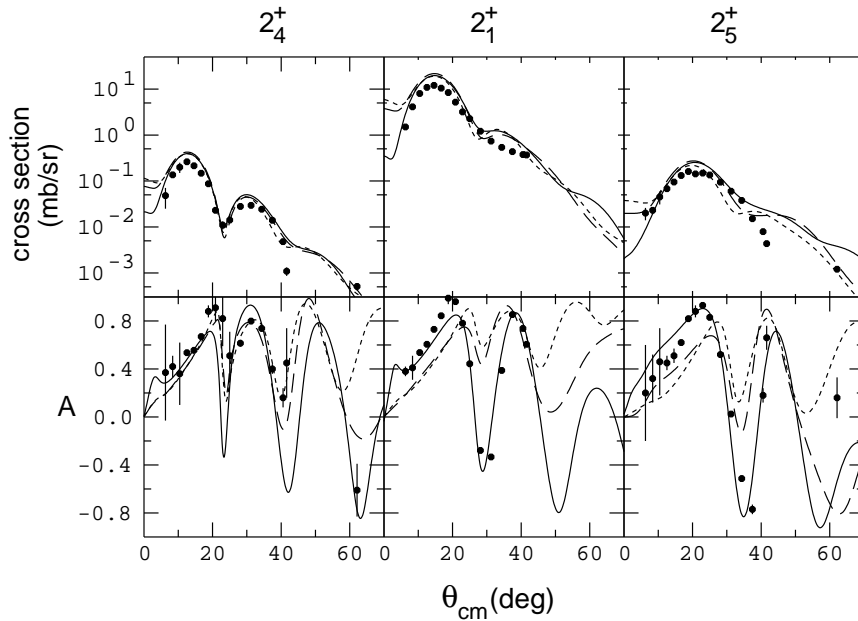


Figure 18. Measurements of the cross section and analyzing power for three 2^+ states in ^{28}Si at 7.933, 1.779, and 8.259 MeV (in order of increasing nuclear density), along with calculations as described in Fig. 15.

here. We also point out that a similar framework has proven successful in microscopic nuclear structure calculations [72]. It must be stressed that relativistic effects of moderate size, such as those we obtain with the effective masses shown in the right panel of Fig. 6, are crucial to obtain a satisfactory description of the main features of the data.

8. Conclusions

The primary focus of this paper has been to establish a reliable basis for inelastic scattering calculations with a medium-modified effective NN interaction. Thus we have concentrated on isoscalar, natural-parity transitions where medium effects from the established many-body models are known to be largest. We have reported our predictions for several such states obtained in (p,p') scattering around 200 MeV.

Our starting interaction is based on a relativistic OBE model, used together with the relativistic Thompson scattering equation. The input OBE potential has been optimized to agree with the best modern sets of phase shift solutions to the NN scattering data base. Medium effects are accounted for via a Dirac-Brueckner many-body approach. The proper handling of the nucleon in the medium through a distorted Dirac wavefunction is well known to provide a crucial saturation mechanism in nuclear matter.

We also report on the conversion of the G-matrix elements to a Yukawa function representation of the effective NN interaction. In this form, it is suitable for use in existing coordinate-space DWIA calculations of (p,p') or (p,n) reactions. This connection also makes a model-dependent separation of the effective NN interaction into direct and exchange pieces.

For practical reasons, the distortions of the nucleon Dirac wavefunction in nuclear matter are often handled in the so-called effective mass approximation. We present a detailed analysis of the central issues involved in this approximation and show that, for nucleon energies in the continuum, appropriate nucleon effective masses are larger (namely, closer to the free space value) than those obtained in typical nuclear matter calculations.

We compare our DBHF predictions with those from the relativistic model of Furnstahl and Wallace and find similar quality for inelastic scattering. For elastic scattering, Furnstahl and Wallace achieve a better agreement with data. This is likely to come from the fact that Furnstahl and Wallace treat nucleons as Dirac bound states in the nucleus, rather than as infinite nuclear matter spinors (as we do).

Some systematic problems still remain with the cross section angular distributions, where the size near the peak is overestimated by about 50%. This problem persists no matter which effective NN interaction we use (except of course for phenomenological ones tuned to best fit the cross section and analyzing power measurements), and may originate in the choice of the DWIA as a reaction mechanism.

We report that a quantitative, relativistic two-body force, combined with a Dirac approach (namely, under the conditions where nuclear matter is well described), captures well the main features of the (p,p') data considered here. We stress again that relativistic effects of moderate size, such as those we obtain

with the effective masses shown on the right side of Fig. 6, are crucial to obtain a satisfactory description of the main features of this data. For future studies involving the spin dependence of the in-medium NN interaction, this model appears to be a satisfactory basis on which to proceed.

We acknowledge the assistance of Malcolm Macfarlane with the transformation from G-matrix to effective NN interaction. This paper was produced with financial assistance from the US NSF under grant NSF-PHY-9602872, a NATO travel grant 900235, and the University of Idaho.

Appendix

This appendix details the transformation between an expansion of the effective NN interaction using Yukawa functions for the direct part and the t- or G-matrix elements generated by the in-medium solution of the NN scattering potential problem.

The Yukawa functions in coordinate space follow the work of Love and Franey [21], and are

$$t_C(r) = \sum_i V_i^C Y(r/R_i), \quad \text{where } Y(x) = e^{-x}/x \quad (\text{A.1a})$$

$$t_S(r) = \sum_i V_i^S Y(r/R_i) \quad (\text{A.1b})$$

$$t_T(r) = \sum_i V_i^T r^2 Y(r/R_i) \quad (\text{A.1c})$$

with the Fourier transforms

$$t_C(k) = 4\pi \sum_i \frac{V_i^C R_i^3}{1 + (kR_i)^2} \quad (\text{A.2a})$$

$$t_S(k) = 8\pi \sum_i \frac{V_i^S k R_i^5}{(1 + (kR_i)^2)^2} \quad (\text{A.2b})$$

$$t_T(k) = 32\pi \sum_i \frac{V_i^T k^2 R_i^7}{(1 + (kR_i)^2)^3}. \quad (\text{A.2c})$$

The S-matrix elements may be derived from the (complex) phase shifts according to

$$S_i = e^{i\delta_i} \quad (\text{A.3a})$$

if the phase is uncoupled, or

$$S_i = \begin{pmatrix} e^{2i\delta_1} \cos 2\epsilon & i e^{i(\delta_1 + \delta_2)} \sin 2\epsilon \\ i e^{i(\delta_1 + \delta_2)} \sin 2\epsilon & e^{2i\delta_2} \cos 2\epsilon \end{pmatrix} \quad (\text{A.3b})$$

if the phase shifts are coupled. Here the quantum numbers i include the total angular momentum J , the total spin S , the total isospin T , and the orbital angular momenta ℓ and ℓ' .

The S-matrix elements are changed into T-matrix elements through the relation

$$S_{\ell'\ell}^{JST}(p) = \delta_{\ell'\ell} - i\kappa t_{\ell'\ell}^{JST}(p). \quad (\text{A.4})$$

The coefficient $\kappa = 2\pi\mu p$ where μ is the reduced mass in the NN system and p is the NN center-of-mass momentum.

The closed form expression for the elements of the transform matrix \mathbf{M} is

$$\begin{aligned}
t_{\ell'\ell}^{JS^T} &= \frac{1}{2p^2} \left(\delta_{\ell'\ell} g_C^{ST}(\ell, p) \right. \\
&\quad - 6\delta_{\ell'\ell} \delta_{S1} (-)^{\ell+J} \left\{ \begin{matrix} \ell & J & 1 \\ 1 & 1 & \ell \end{matrix} \right\} \left[\sum_{\lambda} (2\lambda+1) \langle \lambda 1 0 0 | \ell 0 \rangle^2 \left\{ \begin{matrix} \ell & \ell & 1 \\ 1 & 1 & \lambda \end{matrix} \right\} g_S^T(\lambda, p) \right] \\
&\quad - (-)^{(\ell'-\ell)/2} 2\sqrt{30} \delta_{S1} (-)^{\ell'+J+3} \left\{ \begin{matrix} \ell' & J & 1 \\ 1 & 2 & \ell \end{matrix} \right\} \left[\sqrt{2\ell'+1} \langle \ell' 2 0 0 | \ell 0 \rangle \frac{1}{p^2} (g_T^T(\ell, p) + g_T^T(\ell', p)) \right. \\
&\quad \left. \left. + \sqrt{30} \sum_{\lambda} (2\lambda+1) \langle \lambda 1 0 0 | \ell' 0 \rangle \langle \lambda 1 0 0 | \ell 0 \rangle \left\{ \begin{matrix} \ell' & \ell & 2 \\ 1 & 1 & \lambda \end{matrix} \right\} \frac{1}{p^2} g_T^T(\lambda, p) \right] \right).
\end{aligned} \tag{A.5}$$

The sums on λ run from the maximum of $\ell - 1$ or $\ell' - 1$ to the minimum of $\ell + 1$ or $\ell' + 1$. The Yukawa coefficients are contained in the expressions for the g functions as

$$g_C^{ST}(\ell, p) = \sum_{\alpha} V_{\alpha}^C R_{\alpha} Q_{\alpha}(y_{\alpha}) \tag{A.6a}$$

$$g_S^T(\ell, p) = \sum_{\alpha} V_{\alpha}^S R_{\alpha} Q'_{\alpha}(y_{\alpha}) \tag{A.6b}$$

$$g_T^T(\ell, p) = \sum_{\alpha} V_{\alpha}^T R_{\alpha} Q''_{\alpha}(y_{\alpha}) \tag{A.6c}$$

where the Q_{α} are Legendre functions of the second kind and the derivatives are with respect to y_{α} where

$$y_{\alpha} = 1 + \frac{1}{2p^2 R_{\alpha}^2} \tag{A.6d}$$

The V^C , V^S and V^T are the central, spin-orbit, and tensor Yukawa coefficients, and the R are their associated ranges.

The details of this transform were provided by Malcolm Macfarlane, who derived them as part of an extended study of the off-shell unitarity of the effective NN interaction [73]. While the version here recognizes only one value of the momentum p , an extended version exists that makes the connection to either a half-off-shell or a fully-off-shell t- or G-matrix element.

References

1. K.A. Brueckner, C.A. Levinson, and H.M. Mahmoud, Phys. Rev. **95**, 217 (1954).
2. H.A. Bethe, Phys. Rev. **103**, 1353 (1956).
3. J. Goldstone, Proc. R. Soc. (London) A **239**, 267 (1957).
4. H.A. Bethe, Ann. Rev. Nucl. Sci. **21**, 93 (1971).
5. M.I. Haftel and F. Tabakin, Nucl. Phys. **A158**, 1 (1970).

6. D.W.L. Sprung, *Adv. Nucl. Phys.* **5**, 225 (1972).
7. M.R. Anastasio, L.S. Celenza, W.S. Pong, and C.M. Shakin, *Phys. Rep.* **100**, 327 (1983).
8. R. Brockmann and R. Machleidt, *Phys. Lett.* **149B**, 283 (1984); *Phys. Rev. C* **42**, 1965 (1990).
9. C.J. Horowitz and B.D. Serot, *Phys. Lett.* **137B**, 287 (1984); *Nucl. Phys.* **A464**, 613 (1987).
10. B. ter Haar and R. Malfliet, *Phys. Rep.* **149**, 207 (1987).
11. G.E. Brown, M. Buballa, Zi Bang Li, and J. Wambach, *Nucl. Phys.* **A593**, 295 (1995).
12. G.E. Brown and M. Rho, *Phys. Rev. Lett.* **66**, 2720 (1991); *Phys. Rep.* **269**, 334 (1996).
13. T. Hatsuda and T. Kunihiro, *Phys. Rep.* **247**, 221 (1994), and references therein.
14. E. Bleszynski, M. Bleszynski, and C.A. Whitten, Jr., *Phys. Rev. C* **26**, 2063 (1982).
15. J.M. Moss, *Phys. Rev. C* **26**, 727 (1982).
16. T.N. Taddeucci *et al.*, *Phys. Rev. Lett.* **73**, 3516 (1994).
17. W.G. Love, Amir Klein, M.A. Franey, and K. Nakayama, *Can. J. of Phys.* **65**, 536 (1987).
18. E.J. Stephenson and J.A. Tostevin, in “Spin and Isospin in Nuclear Reactions” eds. S.W. Wissink *et al.* (Plenum, 1991) p. 2.
19. H. Baghaei *et al.*, *Phys. Rev. Lett.* **69**, 2054 (1992).
20. E.J. Stephenson, J. Liu, A.D. Bacher, S.M. Bowyer, S. Chang, C. Olmer, S.P. Wells, and S.W. Wissink, *Phys. Rev. Lett.* **78**, 1636 (1997).
21. W.G. Love and M.A. Franey, *Phys. Rev. C* **24**, 1073 (1981).
22. R. Machleidt, *Adv. Nucl. Phys.* **19**, 189 (1989).
23. James J. Kelly, *Program Manual for LEA*, 1995.
24. H.V. von Geramb, *The interaction Between Medium Energy Nucleons in Nuclei - 1982* (AIP Conf. Proc. **97**, 1983) p. 44.
25. L. Rikus, K. Nakano, and H.V. von Geramb, *Nucl. Phys.* **A414**, 413 (1984).
26. K. Nakayama and W.G. Love, *Phys. Rev. C* **38**, 51 (1988).
27. L. Ray, *Phys. Rev. C* **41**, 2816 (1990).
28. R.J. Furnstahl and S.J. Wallace, *Phys. Rev. C* **47**, 2812 (1993).
29. H. Seifert *et al.* *Phys. Rev. C* **47**, 1615 (1993).
30. Q. Chen, J.J. Kelly, P.P. Singh, M.C. Radhakrishna, W.P. Jones, and H. Nann, *Phys. Rev. C* **41**, 2514 (1990).
31. Jian Liu, E.J. Stephenson, A.D. Bacher, S.M. Bowyer, S. Chang, C. Olmer, S.P. Wells, S.W. Wissink, and J. Lisantti, *Phys. Rev. C* **53**, 1711 (1996).
32. R. Machleidt, *One-boson exchange potentials and nucleon-nucleon scattering*, *Comp. Nucl. Phys. 2 – Nucl. Reactions*, eds. K. Langanke, J.A. Maruhu, and S.E. Koonin (Springer, New York, 1993) p. 1.
33. V.G.J. Stoks *et al.*, *Phys. Rev. C* **49**, 2950 (1994).
34. R. Machleidt, F. Sammarruca, and Y. Song, *Phys. Rev. C* **53**, 1483 (1996).
35. W. Legindgaard, *Nucl. Phys.* **A297**, 429 (1978).

36. T. Cheon and E.F. Redish, Phys. Rev. C **39**, 331 (1989).
37. L.D. Miller and A.E.S. Green, Phys. Rev. C **5**, 241 (1972).
38. J.D. Walecka, Ann. Phys. (N.Y.) **83**, 491 (1974).
39. L.G. Arnold, B.C. Clark, and R.L. Mercer, Phys. Rev. C **19**, 917 (1979).
40. R. Brockmann, Phys. Rev. C **18**, 1510 (1978).
41. C.J. Horowitz and B.D. Serot, Nucl. Phys. **A368**, 503 (1981).
42. B.D. Serot and J.D. Walecka, Adv. Nucl. Phys. **16**, 1 (1986).
43. M. Jaminon, Nucl. Phys. **A402**, 366 (1983).
44. G.R. Satchler, *Direct Nuclear Reactions* (Oxford, 1983) p. 115.
45. M.A. Franey and W.G. Love, Phys. Rev. C **31**, 488 (1985).
46. S. Karataglidis, P.J. Dortmans, K. Amos, and R. de Swiniarski, Phys. Rev. C **52**, 861 (1995).
47. T. Cheon, K. Takayanagi, and K. Yazaki, Nucl. Phys. **A437**, 301 (1985); **A445**, 227 (1985).
48. T. Cheon and K. Takayanagi, Nucl. Phys. **A455**, 653 (1986).
49. A.K. Kerman, H. McManus, and R.M. Thaler, Ann. Phys. **8**, 551 (1959).
50. H. de Vries, C.W. de Jager, and C. de Vries, At. Data and Nucl. Data Tables **36**, 495 (1987).
51. L. Ray and G.W. Hoffman, Phys. Rev. C **31**, 538 (1985).
52. S. Karataglidis, P.J. Dortmans, K. Amos, R. de Swiniarski, Phys. Rev. C **53**, 838 (1996).
53. P.J. Dortmans, K. Amos, and S. Karataglidis, J. Phys. G **23**, 183 (1997).
54. M.A. Suhail, S.M. Saliem, and W. Haider, J. Phys. G **23**, 365 (1997).
55. S.P. Weppner, Ch. Elster, and D. Hüber, Phys. Rev. C **57**, 1378 (1998).
56. E. Bauge, J.P. Delaroche, and M. Girod, Phys. Rev. C **58**, 1118 (1998).
57. H.F. Arellano, F.A. Brieva, and W.G. Love, Phys. Rev. C **52**, 301 (1995).
58. R. Crespo, R.C. Johnson, and J.A. Tostevin, Phys. Rev. C **53**, 3022 (1996).
59. Ch. Elster, S.P. Weppner, and C.R. Chinn, Phys. Rev. C **56**, 2080 (1997).
60. H.O. Meyer *et al.*, Phys. Rev. C **23**, 616 (1981).
61. R.M. de Vries and N. Di Giacomo, J. Phys. G **7**, 751 (1981).
62. H.O. Meyer and P. Schuandt, Phys. Lett. **107B**, 353 (1981).
63. J.A. Tjon and S.J. Wallace, Phys. Rev. C **35**, 280 (1987); Phys. Rev. C **36**, 1085 (1987).
64. J.J. Kelly and S.J. Wallace, Phys. Rev. C **49**, 1315 (1994).
65. C.A. Olmer *et al.*, Phys. Rev. C **29**, 361 (1984).
66. J. Liu, Ph.D. thesis, Indiana University, 1995.
67. for example, F. Rathmann *et al.*, Phys. Rev. C **58**, 658 (1998).
68. M. Lacombe *et al.*, Phys. Rev. C **21**, 861 (1980).
69. F. Sammarruca and E.J. Stephenson, Phys. Rev. C **58**, 307 (1998).
70. R.B. Wiringa *et al.*, Phys. Rev. C **51**, 38 (1995).
71. F. Perey and B. Buck, Nucl. Phys. **32**, 353 (1962).

72. M.F. Jiang *et al.*, Phys. Rev. C **46**, 910 (1992).
73. M.H. Macfarlane and Edward F. Redish, Phys. Rev. C **37**, 2245 (1988).